

Observation of particle acceleration in laboratory magnetosphere

Y. Kawazura, Z. Yoshida, M. Nishiura, H. Saitoh, Y. Yano, T.

Nogami, N. Sato, M. Yamasaki, A. Kashyap and T. Mushiake

Graduate School of Frontier Sciences, The University of Tokyo, Kashiwa, Chiba 277-8561, Japan

(Dated: December 7, 2024)

The self-organization of magnetospheric plasma is brought about by inward diffusion of magnetized particles. Not only creating a density gradient toward the center of a dipole magnetic field, the inward diffusion also accelerates particles and provides a planetary radiation belt with high energy particles. Here, we report the first experimental observation of a ‘laboratory radiation belt’ created in the Ring Trap 1 (RT-1) device. By spectroscopic measurement, we found an appreciable anisotropy in the ion temperature, proving the betatron acceleration mechanism which heats particles in the perpendicular direction with respect to the magnetic field when particles move inward. The energy balance model including the heating mechanism explains the observed ion temperature profile.

Magnetospheres are natural plasma confinement devices ubiquitous in the universe. Yet, their creation mechanism remains to be fully understood. There must be a spontaneous mechanism that transports particles towards the center of a dipole magnetic field [1, 2]. However, such *inward diffusion* seemingly violates the entropy principle, because it creates a gradient instead of flattening the density distribution. This challenge may be overcome by considering adiabatic invariants; the constancy of these invariants poses topological constraints on particle dynamics which ultimately result in the emergence and sustenance of an inhomogeneous state [3–5]. The same mechanism plays another interesting role, i.e., the acceleration of particles to produce a radiation belt [6–10]. Conserving the adiabatic invariants, the kinetic energy of a particle increases when it moves inwards. Here, we report the first experimental observation of a ‘laboratory radiation belt’ created by a superconducting magnet. The key to revealing such an acceleration mechanism is the anisotropy of ion temperatures.

The experiment in question was performed on the Ring Trap 1 (RT-1) device which is a ‘laboratory magnetosphere’ simulated by a levitated superconducting magnet [11, 12]. Figure 1 shows the layout of the device, together with associated plasma images (visible-light image, soft X-ray image and an electron density distribution reconstructed from interferometry). Plasma is produced by electron cyclotron resonance heating (ECH) with an 8.2 GHz microwave (maximum power of 50 kW) and a discharge duration of approximately 1 s. The plasma contains high-temperature ($10 \sim 50$ keV) electrons as well as low temperature ($\lesssim 100$ eV) electrons; typically, the former occupies about half of the total population [13]. The electron density has a peaked radial profile [14, 15]. Similar density profiles were observed in LDX, which is another dipole confinement system; the experiment in LDX identified the creation mechanism as the inward diffusion driven by low-frequency fluctuations [16]. On RT-1, distinct proof of inward diffusion was provided by producing a non-neutral (pure electron) plasma [17]; by action-conserving acceleration, electrons diffuse into the

central region where the electric potential is higher than their initial energies (such particles absorb energy from fluctuations, which drive radial motion).

The basic mechanism of inward diffusion and how it is connected to particle acceleration are depicted as follows: In a dipole magnetic field, the motion of charged particles is hierarchized by three adiabatic invariants; these are the magnetic moment, the bounce action and the longitudinal angular momentum. Typically, the frequencies of the corresponding periodic motions are separated by three orders of magnitude. The third invariant is most fragile, and its violation (i.e. the change of angular momentum) gives rise to the radial transport of particles. When the diffusion of magnetized particles is constrained by the remaining adiabatic invariants, the particle density tends to distribute uniformly on ‘magnetic coordinates’ rather than on Euclidean coordinates. Therefore, the homogeneous density on the former turns out to be inhomogeneous on the latter [4, 5]. Conserving the remaining adiabatic invariants, the kinetic energy of a particle increases as it moves inwards. An increase in cyclotron frequency (maintaining the magnetic moment constant) results in betatron acceleration of the velocity in the direction perpendicular to the magnetic field, and an increase in bounce frequency (maintaining the bounce action constant) results in Fermi acceleration of the parallel velocity [2] (part of the electron is further accelerated to an ultra-relativistic regime by whistler waves [18, 19]). Since the former is stronger than the latter, the inward diffusion results in temperature anisotropy [2].

Numerous satellite observations have provided evidence of anisotropic temperatures in planetary radiation belts. The anisotropic electron temperatures are consistent with the estimates from inward diffusion heating [20–22]; ions also have anisotropic temperatures in the radiation belt of the Earth [23, 24] as well as that of Saturn [25]. The essence of this paper’s investigations into the laboratory radiation belt is anisotropic ion temperature. On RT-1, we found that electrons are confined in a vertically thin region, resembling planetary radiation belts [14]; see Fig. 1b. In the inward diffusion process, a concomitant heating mechanism must be in effect to pro-

duce high-energy electrons. However, electrons are also heated by ECH (cyclotron resonance occurs just in the vicinity of the levitated ring magnet). It is, therefore, difficult to separate the betatron and Fermi accelerations in the total energy balance of electrons. As a viable alternatives, ions may thus be used as an appropriate target for analyzing potential heating mechanisms.

Spatial distribution of ion temperature was measured by two sets of Doppler spectroscopies; one scanned the plasma on a horizontal plane, and the other on a vertical plane (see Fig.1b). The lines of sight of the former ranged from $r = 375$ mm to 878 mm, and those of the latter ranged from $r = 375$ mm to 808 mm on the $z = 0$ axis (r and z are the radial and vertical coordinates, respectively, $r = 375$ mm is the surface of the superconducting magnet, $r = 1000$ mm is the vacuum chamber wall, and $z = 0$ is the mid plane of the magnetic dipole). HeII transition (468.565 nm) was used to measure the Doppler broadening. The horizontal chords measured the perpendicular temperature (T_{\perp}) with respect to the ambient magnetic field, while the vertical chords measured the mixture of T_{\perp} and the parallel temperature (T_{\parallel}). The local temperature profiles of T_{\perp} and T_{\parallel} were reconstructed from the line integrated spectrum data (see Appendix A for the detailed algorithm).

Figure 2 shows the two dimensional profiles of T_{\parallel} and T_{\perp} of the He⁺ ion in helium plasma. Because of the mirror effect, T_{\parallel} decreases and T_{\perp} increases with closer distance to the magnetic poles. The radial temperature profile of the He⁺ ion on the equatorial plane is plotted in Fig. 2c, showing an evident difference between T_{\perp} and T_{\parallel} .

In order to distinguish the effect of betatron acceleration as the preferential heating mechanism for T_{\perp} , the energy balance in the He⁺ ions was examined. By conservation of the magnetic moment, T_{\perp} must increase upon displacement towards the central region as the magnetic field strength increases. From conservation of the first adiabatic invariant, it may be estimated that $\Delta T_{\perp}/T_{\perp} = \Delta B/B$, where B is the magnetic field strength. Let Δr denotes the radial displacement by an infinitesimal time interval Δt . The heating power by betatron acceleration is given by

$$P_{\text{betatron}} \sim \frac{\Delta T_{\perp}}{\Delta t} = T_{\perp} V_r \left| \frac{d \ln B}{dr} \right|, \quad (1)$$

where $V_r = \Delta r/\Delta t$ is the speed of inward diffusion.

A close parallel mechanism is the Fermi acceleration which heats T_{\parallel} via an increase in the bounce frequency. In a point-dipole magnetic field (which may approximate a planetary magnetic field), it is known that betatron acceleration yields much stronger heating than Fermi acceleration [2]. In the magnetic field of RT-1, on the other hand, both of them may yield almost same powers if the first and second actions are equally conserved. But if the constancy of the second action is broken upon inward diffusion, only the betatron acceleration will be in effect.

The decision right is given to the driving mechanism of the inward diffusion.

Figure. 3 shows the frequency spectrum of the density fluctuations detected by a reflectometer. A flat spectrum extending up to around 10 kHz was observed. The bounce frequency of a He⁺ ion is typically around 15 kHz (assuming $T_{\parallel} \sim 10$ eV). On the other hand, the cyclotron frequency is typically 360 kHz (for $T_{\perp} = 20$ eV and $B = 150$ G); thus, the betatron acceleration is deemed to be ideally in effect. Hence, it was concluded that in this instance, the Fermi acceleration is at most very weak in comparison with the betatron acceleration.

Other competitive processes are (1) the thermal equilibration of He⁺ ions and the cold component of electrons, (2) the loss of He⁺ ions by charge exchange with neutral particles and (3) the isotropization of T_{\perp} and T_{\parallel} . The effect of hot electrons may be neglected because the thermal equilibration time is on the order of 10^3 s, which is considerably longer than the lifetime of the plasma. In this instance, no assumption is made of any ‘anomalous transport’; thus, the only energy loss mechanism at play is charge exchange loss.

Taking into account the aforementioned processes, a one-dimensional model of energy transport on the radial coordinate r may be considered:

$$\frac{dT_{\perp}}{dt} = \frac{T_e - T_{\perp}}{\tau_{ei}} - \frac{T_{\perp} - T_{\parallel}}{\tau_{iso}} - \frac{T_{\perp}}{\tau_{cx}} + P_{\text{betatron}}, \quad (2)$$

$$\frac{d}{dt} \left(\frac{T_{\parallel}}{2} \right) = \frac{T_e - T_{\parallel}}{2\tau_{ei}} + \frac{T_{\perp} - T_{\parallel}}{\tau_{iso}} - \frac{T_{\parallel}}{2\tau_{cx}}, \quad (3)$$

where d/dt is the temporal derivative to be evaluated on each volume element co-moving with the plasma on a Lagrangian coordinate; for a stationary state, we may evaluate $d/dt = V_r d/dr$ with an inward diffusion speed V_r . All coefficients of equations (2) and (3) are evaluated by experimentally measured local plasma parameters.

The electron-ion thermal equilibration time (τ_{ei}) is a function of the ion temperature (~ 10 eV), the electron temperature (which is homogeneously 30 eV) measured by the HeI line intensity ratio [26] and the cold electron density [27] ($\sim 10^{17} \text{ m}^{-3}$). This time was determined to be ~ 0.1 s. The ion isotropization time (τ_{iso}) is on the order of 1 ms, as estimated by the ion temperatures ($T_{\perp} \sim 20$ eV and $T_{\parallel} \sim 10$ eV) and the density [27].

Let us estimate neutral helium gas density profile to evaluate the time constant τ_{cx} which scales the time of charge transfer between the He⁺ ion and the neutral helium gas. The penetration length of the neutral particle is $\lambda = v_n/n_e \langle \sigma v \rangle_{\text{ion}}$, where v_n is the thermal velocity of the neutral gas and $\langle \sigma v \rangle_{\text{ion}}$ is the ionization rate. Since electron temperature is spatially homogeneous with 30 eV from HeI line intensity ratio measurement, $\langle \sigma v \rangle_{\text{ion}}$ is spatially constant. We show the radial profile of the

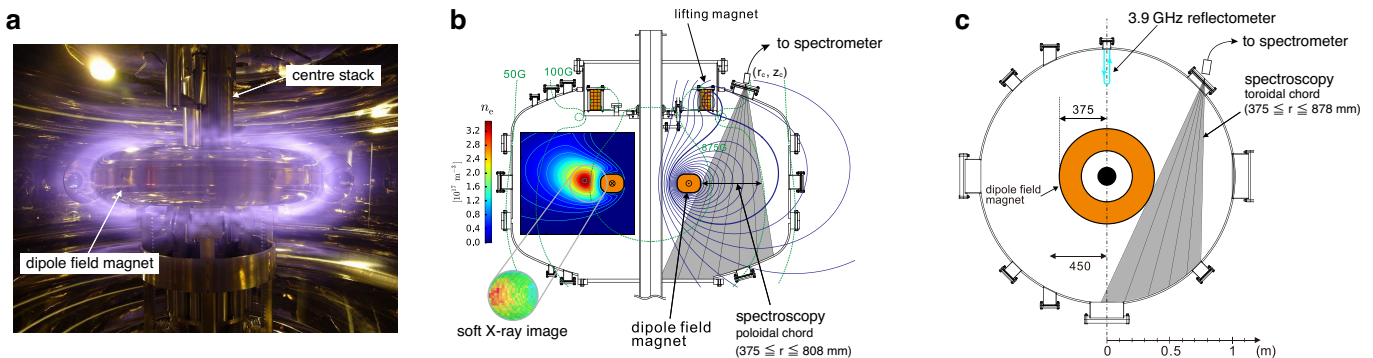


FIG. 1: **Experimental set-up.** (a) Visible-light photograph image of the plasma in RT-1. The light (mainly the Balmer series lines) is emitted by neutral particles that are remaining in the plasma. The high-temperature plasma is confined to the outer region, creating a ‘radiation belt’ (the soft X-ray image is shown in the next figure). (b) The plan (vertical front view) of the device. The superconducting magnet is levitated by the lifting magnet placed on the top of the vacuum chamber. On the right-hand side of the figure, the magnetic field lines are plotted by solid lines. The lines of sight of the vertical spectroscopic measurement cover the greyed vertical plane. On the left-hand side of the figure, the electron density profile (measured by interferometers [14, 15]) is plotted and the superimposed soft X-ray image (the interferometry measurement and the soft X-ray image are from different shots) is shown. The density profile is vertically compressed, indicating the mirror effect along magnetic field lines; by the diamagnetism, magnetized particles prefer to stay in the weaker-field equatorial region. (c) The plan (top view) of the device. The lines of sight of the horizontal spectroscopic measurement cover the greyed horizontal plane. The reflectometer (3.9 GHz microwave) measures the density fluctuation near the cutoff density which is $\sim 1.9 \times 10^{17} \text{ m}^{-3}$ (light blue).

line averaged neutral He gas temperature estimated by the Doppler broadening of the HeI (471.315 nm) line in Fig. 4, which exhibits that the neutral He temperature is almost spatially homogeneous with 0.7 eV; therefore λ only depends on n_e . Using the electron density of the shot in Fig. 2, λ is evaluated as ~ 1 m near the internal coil and ~ 10 m at the chamber wall, implying that the neutral gas density is spatially flat. The flat profile of neutral He was double-checked by emission intensity of HeI line, and accordingly verified. The emission intensity is evaluated as $I_n \propto n_e n_n \langle \sigma v \rangle_{\text{exc}}$, where $\langle \sigma v \rangle_{\text{exc}}$ is the excitation rate of He^{0+} . Since the electron temperature and the neutral gas density are spatially constant, I_n is proportional to n_e . Figure 5 shows the profile of n_e and the measured HeI line intensity. Both profiles were found to be consistent. Figure 6 shows the ionization ratio of He obtained by solving the rate equation of ionization, recombination and charge exchange processes. Since adequate light emission was observed from both the HeI and HeII lines, the neutral gas density was determined to be roughly in the range $0.1n_e \lesssim n_n \lesssim 10n_e$. Therefore, the neutral He gas density is homogeneously $n_n = 1 \times 10^{17} \text{ m}^{-3}$. Using the ADAS code [28], τ_{cx} was determined to be ~ 1 ms.

The inward diffusion speed V_r is required to evaluate P_{betatron} . This was measured in the initial formation phase. At the beginning of the discharge, the density has a broad distribution, but subsequently it begins to concentrate into the central region, thereby creating a clump of particles. Figure 7 shows the time evolution of the line integrated electron density measured by the three chord interferometers around the onset of the plasma dis-

charge. Two dimensional density profile of n_e is reconstructed at the two different time points $t = 0.98300$ s and $t = 0.98348$ s. The electron density evolves in accordance with the continuity equation with the inward diffusion velocity \mathbf{V} :

$$\frac{\partial n_e}{\partial t} + \frac{1}{r} \frac{\partial}{\partial t} (r n_e V_r) + \frac{\partial}{\partial z} (n_e V_z) = 0. \quad (4)$$

We assume \mathbf{V} as

$$\mathbf{V} = V_{\psi 0} \left(\frac{\psi}{\psi_1} \right)^\alpha \frac{\nabla \psi}{|\nabla \psi|}. \quad (5)$$

The parameters $V_{\psi 0}$ and α are optimized so that the solution of (4) with the initial condition as n_e at $t = 0.98300$ in Fig. 7 becomes closer to n_e at $t = 0.98348$. Choosing appropriate parameters, the density evolution is replicated well, as shown in Fig. 7, thus the speed V_r that transports the particles is deduced. In the stationary phase, we do not have a direct measurement of V_r , but we assume that the same estimate applies.

Equations (2) and (3) are both ultimately solved with the aforementioned parameters. An initial condition at $r = 1000$ mm (edge of the plasma) is assumed; using the measurement, $T_\perp = T_\parallel = 8$ eV. The solution is shown in Fig. 8b. and it turns out that the model explains the experimental profiles presented in Fig. 2c. Here the exact value of the neutral gas density (which has a homogeneous distribution in the plasma) is tuned to $1 \times 10^{17} \text{ m}^{-3}$ to match the peak value of T_\perp .

The energy balance model is put to the test by comparing the parameter dependencies of the solutions and

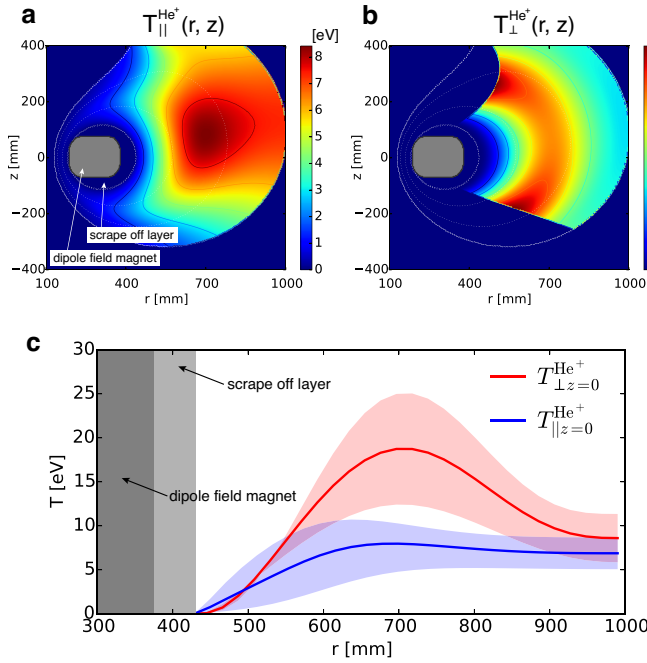


FIG. 2: **Anisotropic ion temperatures in the laboratory radiation belt.** Two dimensional profiles of (a) parallel temperature (T_{\parallel}) and (b) perpendicular temperature (T_{\perp}) of He^+ ions. The white dotted lines show the magnetic field lines. T_{\perp} is plotted in a region where the mirror ratio (the local magnetic field normalized by the minimum magnetic field along each field line) is less than 2. (c) The radial temperature profile on the equatorial plane ($z = 0$). The translucent regions are the error bands estimated by the covariance of the reconstruction fitting. The anisotropy ($T_{\perp} > T_{\parallel}$) becomes maximum in the middle of the confinement region ($r \sim 700$ mm).

experimental scaling laws. Figure 9 shows the dependencies of line averaged temperatures at two different radial points ($r \sim 0.51$ m and $r \sim 0.71$ m). Figures 9a-b illustrate dependence on ECH power, with both the temperature and its anisotropy increasing as ECH power increases. This is consistent with the estimate of betatron heating power (1). The increase in the ECH power implies an increase in the initial ion temperature through the relaxation between cold electrons; then P_{betatron} becomes larger, resulting in larger T_{\perp} and anisotropy. The increase in T_{\parallel} is explained by the increase in the initial temperature and isotropization. Figures 9c-d show the dependence on neutral gas density, which is estimated by the ideal gas equation of state with a temperature of 300 K and the subtraction of electron density. From Fig. 9c, it is seen that ion temperature decreases as the neutral He gas density increases. Therefore the dominant energy loss is considered to be the charge exchange with the neutral gas. This conclusion is consistent with equations (2) and (3). Likewise, from Fig. 9d, the anisotropy decreases as the neutral He gas density increases. Since the inward diffusion heating power P_{betatron} is indepen-

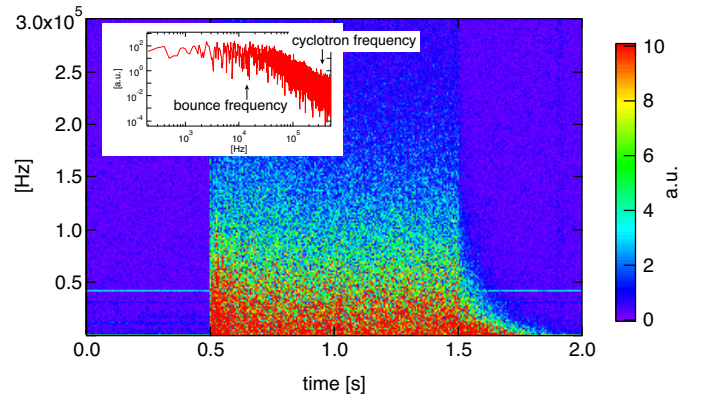


FIG. 3: **Frequency spectrum of the density fluctuations.** Time evolution of the frequency spectrum, measured by the reflectometer, is shown for the total lifetime of the plasma (ECH power is injected from 0.5 s through 1.5 s). The density cutoff resides at $r \sim 640$ mm. The inset is the clip between $t = 1.001584$ s and $t = 1.063193$ s. The fluctuation has a flat spectrum up to around 30 kHz (which ranges beyond the bounce frequency). However, the fluctuations in the range of the ion cyclotron frequency are very weak.

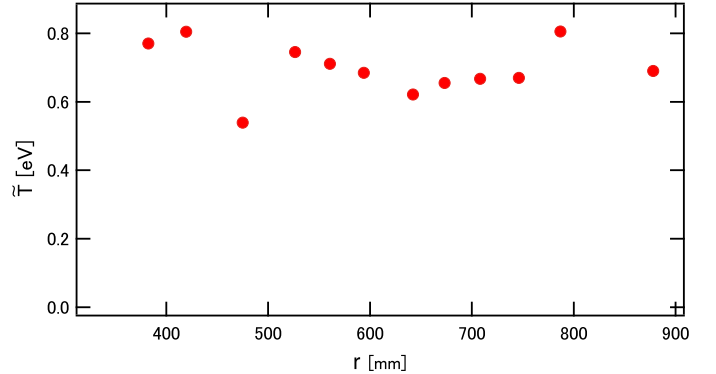


FIG. 4: Radial profile of the line averaged temperature of He^{0+} evaluated from the Doppler broadening of the He I line spectrum (471.315 nm) on the horizontal line of sight.

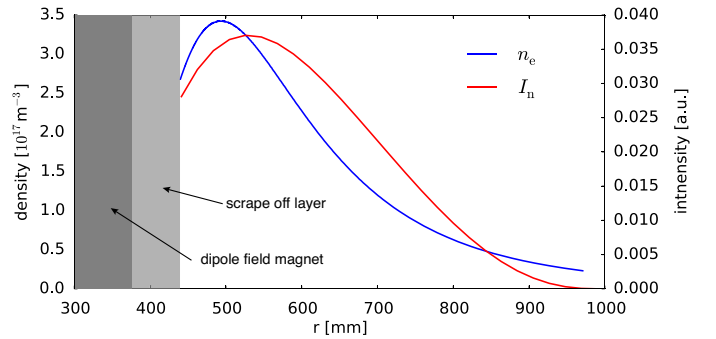


FIG. 5: Radial profiles of n_e and He I (471.315 nm) line emission intensity measured by the horizontal line of sight. n_n and n_e are the same as those in Fig. 8a.

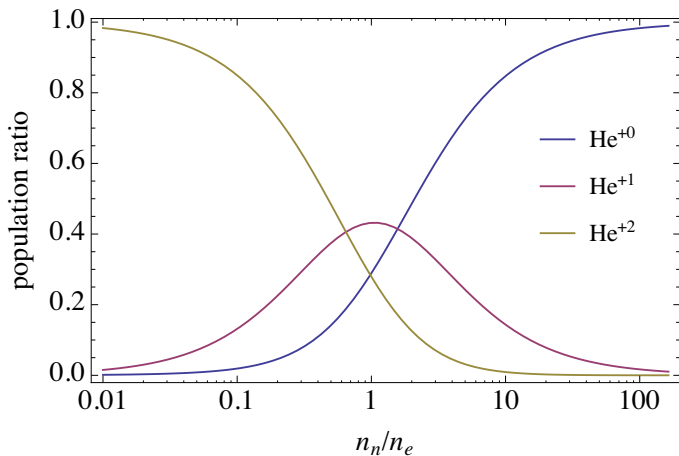


FIG. 6: Ionization ratio of He as a function of neutral particle density, obtained by solving the rate equation of ionization, recombination and charge exchange processes. The electron temperature is assumed to be 30 eV.

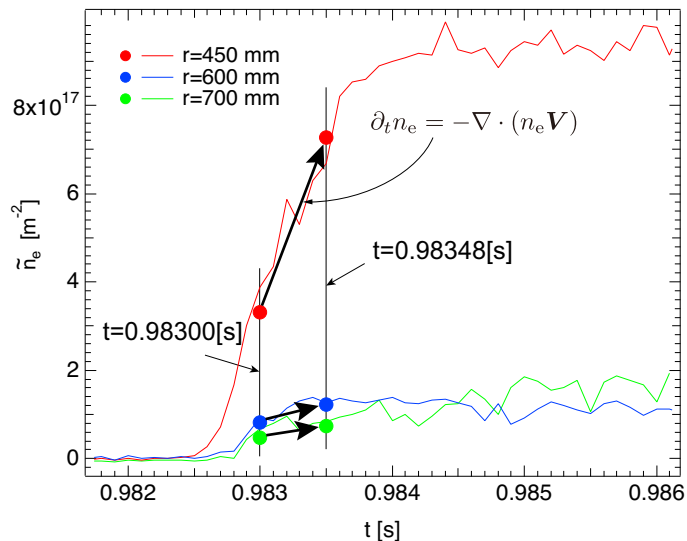


FIG. 7: Time evolution of the line integrated electron density measured by the interferometers at each chords around the onset of the plasma discharge. The bullets at $t = 0.98348$ s are the solution of (4) with the parameters $(V_{\psi 0}, \alpha) = (3000, -7)$ and the initial condition as the bullets at $t = 0.98300$ s.

dent of the neutral gas density, an increase in the charge

exchange loss results in small anisotropy. Therefore all the dependencies were found to be consistent with the assessed model underpinning this study.

In conclusion, the anisotropic ion temperature observed in the laboratory radiation belt is experimental proof of the betatron acceleration concomitant with inward radial diffusion of particles.

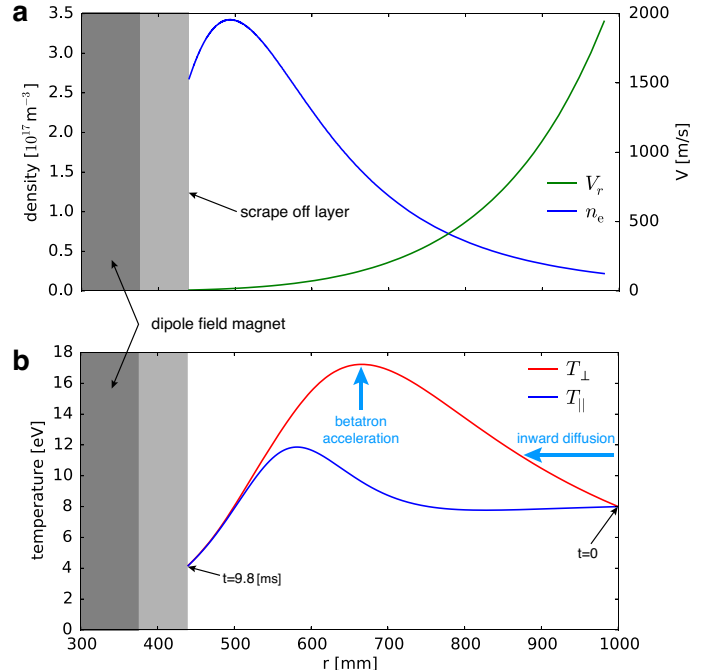


FIG. 8: Simulation of the anisotropic ion temperature by the energy transport model. (a) Radial distribution of the inward diffusion speed V_r and the electron density n_e . V_r is determined by the evolution of the density. n_e is determined by the interferometry measurement. Other coefficients in the energy balance model (2)–(3) are determined by the measurements of local plasma parameters. (b) The radial profiles of T_{\perp} and T_{\parallel} calculated by the energy balance model (2)–(3). The result is compared with the experimental observation shown in Fig 2c.

Acknowledgments

We appreciate the helpful comments and suggestions by Dr. Shinichiro Kado. This work was supported by JSPS KAKENHI Grant No. 23224014.

- [1] Schulz, M. & Lanzerotti, L. J. Particle Diffusion in the Radiation Belts (Springer, 1974).
- [2] Dessler, A. J., ed. Physics of the Jovian magnetosphere. **3**. (Cambridge University Press, 2002).
- [3] Birmingham, T. J., Northrop, T. G. & Fälthammar, C.-G. Charged Particle Diffusion by Violation of the Third

- Adiabatic Invariant. *Phys. Fluids* **10**, 2389-2398 (1967)
- [4] Hasegawa, A. Motion of a Charged Particle and Plasma Equilibrium in a Dipole Magnetic Field Can a Magnetic Field Trap a Charged Particle? Can a Magnetic Field Having Bad Curvature Trap a Plasma Stably? *Phys. Scr. T* **116**, 72 (2005).

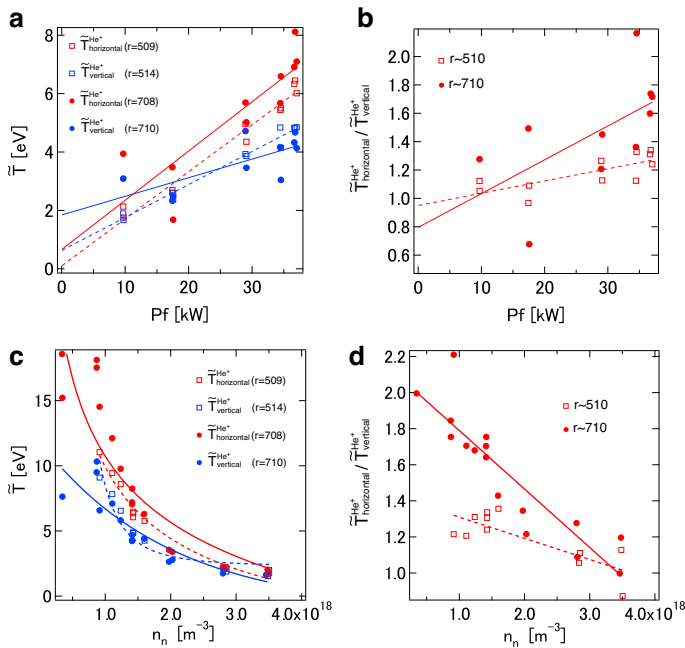


FIG. 9: Dependence of (a) the line averaged temperature of He^+ and (b) the anisotropy on the ECH power, and the dependence of (c) the line averaged temperature and (d) the anisotropy on the neutral He gas density. The temperature and its anisotropy are measured at two fixed radial point ($r \sim 0.51$ m and $r \sim 0.71$ m). The solid and broken lines indicate the line fitting for (a), (b) and (d), and power function fitting for (c).

[5] Yoshida, Z. & Mahajan, S. M. Self-organization in foliated phase space: construction of a scale hierarchy by adiabatic invariants of magnetized particles. *Prog. Theor. Exp. Phys.* **2014**, 073J01 (2014).

[6] Kellogg, P. J. Van Allen Radiation of Solar Origin. *Nature* **183**, 1295-1297 (1959).

[7] Brice, N. & McDonough, T. R. Jupiter's radiation belts. *Icarus* **18**, 206-219 (1973).

[8] Coroniti, F. V. Energetic electrons in Jupiter's magnetosphere. *Atrophys J. Suppl. Ser.* **27**, 261 (1974).

[9] Nishida, A. Outward diffusion of energetic particles from the Jovian radiation belt. *J. Geophys. Res.* **81** 1771-1773 (1976).

[10] Carbary, J. F., Hill, T. W., Dessler, A. J. Planetary spin period acceleration of particles in the Jovian magnetosphere. *J. Geophys. Res.* **81** 5189-5195 (1976).

[11] Yoshida, Z. *et al.* First Plasma in the RT-1 Device. *J. Plasma Fusion Res.* **1**, 008 (2006).

[12] Yoshida, Z. *et al.* Self-organized confinement by magnetic dipole: recent results from RT-1 and theoretical modeling. *Plasma Phys. Control. Fusion* **55**, 014018 (2013).

[13] Saitoh, H. *et al.* High- β plasma formation and observation of peaked density profile in RT-1. *Nucl. Fusion* **51**, 063034 (2011).

[14] Saitoh, H. *et al.* Observation of a new high-beta and high-density state of a magnetospheric plasma in RT-1. *Phys. Plasmas* **21**, 082511 (2014).

[15] Saitoh, H. *et al.* Measurement of a density profile of a hot-

electron plasma in RT-1 with three-chord interferometry. *Phys. Plasmas* **22**, 024503 (2015).

[16] Boxer, A. C. *et al.* Turbulent inward pinch of plasma confined by a levitated dipole magnet. *Nature Phys.* **6**, 207 (2010).

[17] Yoshida, Z. *et al.* Magnetospheric Vortex Formation: Self-Organized Confinement of Charged Particles. *Phys. Rev. Lett.* **104**, 235004 (2010).

[18] Chen, Y., Geoffrey D. R. & Reiner H. W. F. The energization of relativistic electrons in the outer Van Allen radiation belt. *Nature Phys.* **3**, 614-617 (2007).

[19] Horne, R. B. *et al.* Gyro-resonant electron acceleration at Jupiter. *Nature Phys.* **4**, 301-304 (2008).

[20] Bolton, S. J., Thorne, R. M., Gurnett, D. A., Kurth, W. S. & Williams, D. J. Enhanced whistler-mode emissions: Signatures of interchange motion in the Io torus. *Geophys. Res. Lett.* **24**, 2123-2126 (1997).

[21] Thorne, R. M. *et al.* Galileo evidence for rapid interchange transport in the Io torus. *Geophys. Res. Lett.* **24**, 2131-2134 (1997).

[22] Xiao, F., Thorne, R. M., Gurnett, D. A. & Williams, D. J. Whistler-mode excitation and electron scattering during an interchange event near Io. *Geophys. Res. Lett.* **30**, 1749 (2003).

[23] Olsen, R.C. Equatorially Trapped Plasma Populations. *J. Geophys Res.*, **86**, 235-245, (1981).

[24] Olsen, R. C. *et al.* Plasma Observations at the Earth's Magnetic Equator. *J. Geophys Res.*, **92**, 2385-2407, (1987).

[25] Persoon, A. M. *et al.* A diffusive equilibrium model for the plasma density in Saturn's magnetosphere. *J. Geophys. Res.* **114** A0421 (2009).

[26] Schweer, B., Mank, G., Pospieszczyk, A., Brosda, B., & Pohlmeier, B. Electron temperature and electron density profiles measured with a thermal He-beam in the plasma boundary of TEXTOR. *J. Nucl. Mater.* **196**, 174 (1992).

[27] Huba, J. D. NRL Plasma Formulary (Naval Research Laboratory, Washington DC, 1994)

[28] <http://www.adas.ac.uk>.

Appendix A: ALGORITHM FOR THE RECONSTRUCTION OF THE LOCAL PROFILE

To reconstruct the local temperature profile from the line averaged measured data, the following procedure was used. The local profile on the equatorial plane ($z = 0$) is reconstructed from the spectrum data obtained via the horizontal chord. From the axisymmetric property, the spectrum on the equatorial plane can be written as $f_{\text{eq}}(\lambda, \psi(r, 0))$ where λ is the wavelength, $\psi(r, z)$ is the inverse of magnetic flux and r and z are the radial and vertical coordinates, respectively. The innermost flux surface contacting the dipole field magnet is denoted as ψ_0 , and the outermost flux contacting the vacuum chamber at $r = 1000$ mm is denoted as ψ_1 . Hereafter, the subscript eq means the value on the equatorial plane. The line integrated spectrum $g_{\text{eq}}(\lambda, y)$ is thus calculated from the local spectrum as

$$g_{\text{eq}}(\lambda, y) = 2 \int_0^1 f_{\text{eq}}(\lambda, \psi_{\text{eq}}(\sqrt{x^2 + y^2})) dx, \quad (\text{A1})$$

where x denotes the auxiliary coordinate along the line of sight. We assume

$$f_{\text{eq}}(\lambda, \psi_{\text{eq}}(r)) = \begin{cases} \mathcal{A}_{\text{eq}}(\psi_{\text{eq}}(r)) \exp \left[- \left(\frac{\lambda - \lambda_0 - \mathcal{B}_{\text{eq}}(\psi_{\text{eq}}(r))}{\mathcal{C}_{\text{eq}}(\psi_{\text{eq}}(r))} \right)^2 \right] & (\psi_0 \leq \psi_{\text{eq}}(r) \leq \psi_1) \\ 0 & (\psi_1 \leq \psi_{\text{eq}}(r)) \end{cases},$$

where λ_0 is the central wavelength. The intensity $\mathcal{A}_{\text{eq}}(\psi_{\text{eq}}(r))$ and the shift $\mathcal{B}_{\text{eq}}(\psi_{\text{eq}}(r))$ are assumed to be

$$\begin{aligned} \mathcal{A}_{\text{eq}}(\psi_{\text{eq}}(r)) &= a_1 \frac{(\psi_{\text{eq}}/\psi_0 - 1)^{a_2} (1 - \psi_{\text{eq}}/\psi_1)^{a_3}}{(\psi^*/\psi_0 - 1)^{a_2} (1 - \psi^*/\psi_1)^{a_3}} \quad \left(\psi^* = \frac{a_3 \psi_0 + a_2 \psi_1}{a_2 + a_3} \right) \\ \mathcal{B}_{\text{eq}}(\psi_{\text{eq}}(r)) &= b_1 + b_2 \psi_{\text{eq}} + b_3 \psi_{\text{eq}}^2, \end{aligned}$$

with the perpendicular temperature on the equatorial plane assumed to be

$$T_{\perp \text{eq}}(\psi_{\text{eq}}) = (t_1 - 0.5t_4) \frac{(\psi_{\text{eq}}/\psi_0 - 1)^{t_2} (1 - \psi_{\text{eq}}/\psi_1)^{t_3}}{(\psi^\dagger/\psi_0 - 1)^{t_2} (1 - \psi^\dagger/\psi_1)^{t_3}} + 0.5t_4 \left[1 + \text{erf} \left(\frac{\psi - \psi^\dagger}{0.2(\psi_1 - \psi_0)} \right) \right] \quad \left(\psi^\dagger = \frac{t_3 \psi_0 + t_2 \psi_1}{t_2 + t_3} \right). \quad (\text{A2})$$

The Doppler broadening $\mathcal{C}_{\text{eq}}(\psi_{\text{eq}})$ is determined by $T_{\perp \text{eq}}(\psi_{\text{eq}})$. The functions \mathcal{A}_{eq} , \mathcal{B}_{eq} and $T_{\perp \text{eq}}$ indicate that the spectral emission is zero at both boundaries, the temperature is zero at $\psi = \psi_0$ and t_1 at $\psi = \psi_1$, and the toroidal flow speed may be finite at both boundaries. The observed spectrum data set for the horizontal chord is written as $(\lambda_i, y_j, g_{\text{eq}ij})$. The parameters $(a_1, a_2, a_3, b_1, b_2, b_3, t_1, t_2, t_3, t_4)$ are optimized so as to minimize $|g_{\text{eq}ij} - g_{\text{eq}}(\lambda_i, y_j)|$ for each λ_i and y_j .

Next we build a vertical reconstruction algorithm. Using \mathcal{A}_{eq} and T_{eq} obtained by the horizontal reconstruction, a two-dimensional profile is reconstructed. The position of the collimator is denoted as (r_c, z_c) (Fig. 1b in the primary text). The line of sight passing the equatorial point $(y, 0)$ is given as

$$r = \frac{r_c - y}{z_c} (z - z_c) + r_c. \quad (\text{A3})$$

The line integrated spectrum $g(\lambda, y)$ is calculated from the local spectrum $f(\lambda, r, z)$ as

$$g(\lambda, y) = \int_{-z_c}^{z_c} f(\lambda, r(z), z) \sqrt{1 + \left(\frac{dr}{dz} \right)^2} dz. \quad (\text{A4})$$

In the same manner as the horizontal reconstruction, the local spectrum is assumed to be

$$f(\lambda, r, z) = \begin{cases} \mathcal{A}(r, z) \exp \left[- \left(\frac{\lambda - \lambda_0}{\mathcal{C}(r, z)} \right)^2 \right] & (\psi_0 \leq \psi \leq \psi_1) \\ 0 & (\psi_1 \leq \psi) \end{cases},$$

In the vertical chord, the Doppler shift can be ignored because of the absence of the mean poloidal flow in the dipole magnetic field configuration. We use the magnetic field coordinate to treat the vertical direction, and assume $\mathcal{A}(r, z)$ to be the power function of the magnetic field strength B .

$$\mathcal{A}(r, B(r, z)) = \mathcal{A}_{\text{eq}}(\psi_{\text{eq}}) \left[\frac{B(r, z)}{B_{\text{eq}}} \right]^{-\bar{a}} \quad (\text{A5})$$

where B_{eq} is the magnetic field strength of the same field line on the equatorial plane. In the $z \neq 0$ region, the effective temperature (T_{eff}) causing the Doppler broadening is a combination of T_{\perp} and T_{\parallel} . Defining the angle θ between the line of sight and the line normal to the magnetic field, we may write

$$(T_{\text{eff}})^2 = (T_{\perp} \cos \theta)^2 + (T_{\parallel} \sin \theta)^2. \quad (\text{A6})$$

In the same manner as (A5), we assume the perpendicular temperature profile as

$$T_{\perp}(r, B(r, z)) = T_{\perp\text{eq}} \left(\frac{B}{B_{\text{eq}}} \right)^{\tilde{c}_1}. \quad (\text{A7})$$

While $T_{\perp\text{eq}}$ is already determined by the horizontal reconstruction, we need the profile of T_{\parallel} on the equatorial plane. We assume $T_{\parallel\text{eq}}$ in a similar manner as $T_{\perp\text{eq}}$:

$$T_{\parallel\text{eq}}(\psi_{\text{eq}}(r)) = (\tilde{t}_1 - 0.5\tilde{t}_4) \frac{(\psi_{\text{eq}}/\psi_0 - 1)^{\tilde{t}_2} (1 - \psi_{\text{eq}}/\psi_1)^{\tilde{t}_3}}{(\psi^{\ddagger}/\psi_0 - 1)^{\tilde{t}_2} (1 - \psi^{\ddagger}/\psi_1)^{\tilde{t}_3}} + 0.5\tilde{t}_4 \left[1 + \text{erf} \left(\frac{\psi - \psi^{\ddagger}}{0.2(\psi_1 - \psi_0)} \right) \right] \left(\psi^{\ddagger} = \frac{\tilde{t}_3\psi_0 + \tilde{t}_2\psi_1}{\tilde{t}_2 + \tilde{t}_3} \right). \quad (\text{A8})$$

In the same manner as (A5) and (A7), we assume

$$T_{\parallel}(r, B(r, z)) = T_{\parallel\text{eq}} \left(\frac{B}{B_{\text{eq}}} \right)^{-\tilde{c}_2}. \quad (\text{A9})$$

We write the observed spectrum data set for the vertical chord as (λ_i, y_j, g_{ij}) . The parameters $(\tilde{a}, \tilde{c}_1, \tilde{c}_2, \tilde{t}_1, \tilde{t}_2, \tilde{t}_3, \tilde{t}_4)$ are optimized to minimize $|g_{ij} - g(\lambda_i, y_j)|$ for each λ_i and y_j . A two-dimensional profile of $\mathcal{A}(r, z)$, $T_{\perp}(r, z)$ and $T_{\parallel}(r, z)$ is then ultimately obtained.

Figure 10 shows the fitting precision of Fig. 2c in the primary text. The solid lines are the line averaged temperatures estimated by $g_{\text{eq}}(\lambda, y)$ and $g(\lambda, y)$, respectively, with optimized parameters, while the bullets are the line averaged temperatures estimated by the measured data $g_{\text{eq } ij}$ and g_{ij} , respectively. The translucent regions are the error bands determined by multiplying a constant by the covariance of the reconstruction fitting. The corresponding error bands for the local profile are illustrated in Fig. 2c in the primary text.

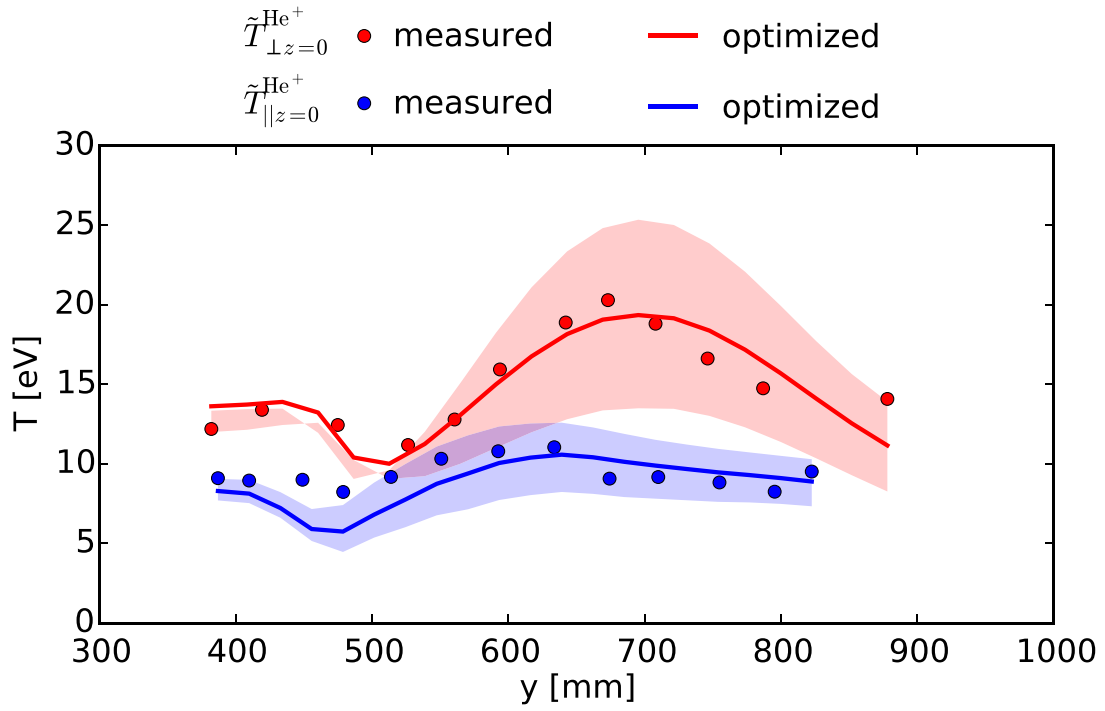


FIG. 10: Line averaged temperature profile to estimate the fitting precision. The bullets are the line averaged temperatures of He⁺ estimated by the measured spectrum data. The solid lines are the line averaged temperatures estimated by the optimized g . The translucent regions are the error bands determined by multiplying a constant by the covariance of the reconstruction fitting.